Transactions of the SMiRT 27
Yokohama, Japan, March 3-8, 2024
Division V

STUDY ON A CRASH SIMULATION MODEL FOR THE MEMBER OF FLEXIBLE STRUCTURE

Miyako Kuwamura[1], Kunio Takekoshi[2]

[1] Assistant Manager, Terrabyte Co., Ltd, Tokyo, Japan (miyako.kuwamura@terrabyte.co.jp)
[2] Division Manager, Terrabyte Co., Ltd, Tokyo, Japan (kunio.takekoshi@terrabyte.co.jp)

ABSTRACT

Protective structures as rope nets and sheets/plates have been used against tornado debris in nuclear power plants. However, modelling methods of such flexible structures for numerical simulations have not been studied as much as structures like protective concrete walls. To validate the proposed modelling methods, a comparative study of a rope net subjected to a drop weight impact has been carried out to identify factors that have a significant impact in modelling. Furthermore, to compare the energy absorption of different flexible protective structures, a comprehensive study of both rope nets and sheets/plates subjected to drop weight impacts has been carried out. The simulation results shows that both materials have the same level of energy absorption, but the aramid fibre sheet alone had a high possibility of rupture. The steel plate has the lowest deformation and the least load on the steel frame.

INTRODUCTION

The Nuclear Regulation Authority of Japan introduced the new regulatory requirements in 2013 for the safety evaluation of nuclear facilities. According to these requirements, safety facilities must not impair safety functions in the event of tornadoes or other anticipated natural events. Protective structures as rope nets and sheets/plates have been used against tornado debris in nuclear power plants. However, energy absorption of such flexible structures has not been exhaustively studied. In this study, a crash simulation model based on a free drop test on a tornado protection net (Aizawa et al., 2021) has been considered. Furthermore, the energy absorption effects of the different materials used for the flexible protective structures have been compared.

OVERVIEW OF THE EXPERIMENT

To develop a lightweight, high-strength tornado protection net, free drop tests were conducted on aramid fibre rope nets at several scales (Aizawa et al., 2021). The medium-size net used in the free drop facility is shown in Figure 1. The inner layer of the rope was made of aramid fibre, while the outer layer of the rope was made of low-density polyethylene. The ropes were not braided together but were restrained by a raschel net. The impactor had a mass of approximately 1000 kg, the same as the designed flying object (a station wagon) for tornado. The drop height of the impactor was used as a parameter. The maximum tension of the ropes and the impact load calculated from the accelerometer of the weight from the test results are shown in Table 1.

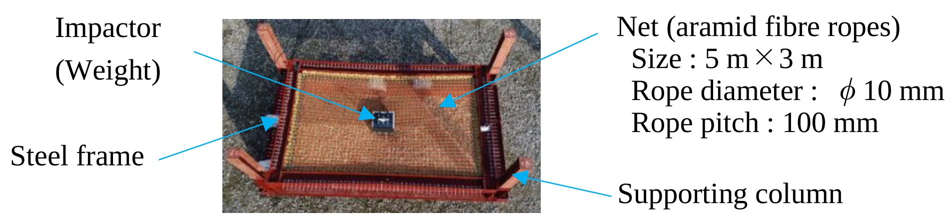

Figure 1. The free drop test using the impactor

Table 1: Results of the free drop test

Drop height [m]	Maximum tension of ropes [kN]	Impact load [kN]
2.5	34.9	208.2
3.5	41.8	260.6
4.5	45.4	306.8

STUDY ON SIMULATION MODEL

A comparative study using LS-DYNA has been conducted on a rope net subjected to a drop weight impact, aiming to investigate crucial modelling conditions.

Simulation Model

The numerical simulation model for the drop test is shown in Figure 2, where the rope net, the steel frame, and the impactor are modelled using beam, shell, solid finite elements, respectively. In the free drop test, the ropes were bound together by a russet net. To simplify the modelling in the simulations, the intersections of the ropes are represented with shared nodes.

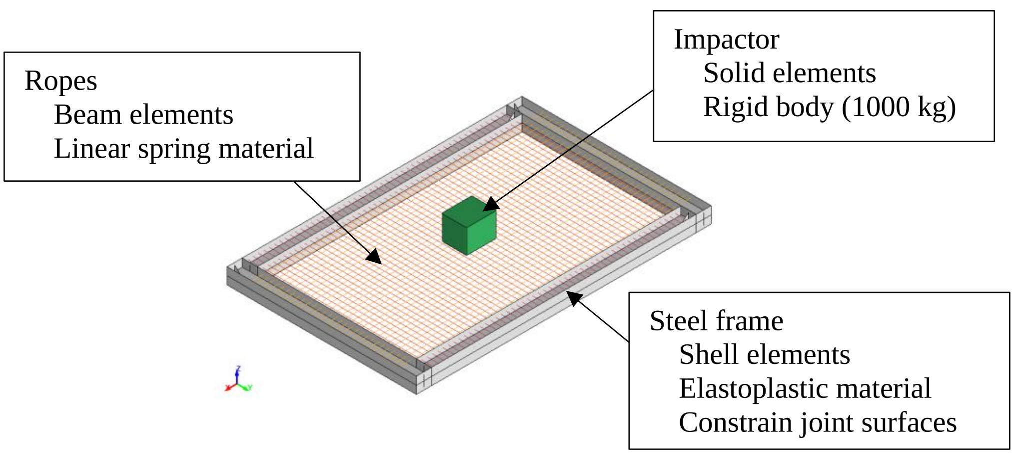

Figure 2. Simulation model for the rope net

Linear springs are used for modelling the ropes, and the compressive stiffness is also considered. Elastoplastic material is applied to the steel frame. The true stress-true strain relationship for the steel frame is determined by referring to the Guidelines for Tornado Missile (JSME S NX6-2019) and applying an estimation formula proposed by ASME B&PV Code Sec. VIII (2011 Addenda) Div. 2, Annex 3-D. The yield stress, considering the strain rate dependence, is defined using an estimation formula proposed by The Japan Welding Engineering Society, as follows:

$$\sigma_y = \sigma_{y0}(T_0) \cdot \exp\left[8 \times 10^{-4} \cdot T_0 \cdot \left(\frac{\sigma_{y0}(T_0)}{E}\right)^{-1.5} \cdot \left\{\frac{1}{T \cdot \ln(10^8/\dot{e})} - \frac{1}{T_0 \cdot \ln(10^8/\dot{e}_0)}\right\}\right] \quad (1)$$

where $\sigma_{y0}(T_0)$, T_0 , $\dot{e}_0$, and E represent the yield stress (MPa), temperature (K), strain rate (1/s), and longitudinal elastic modulus (MPa) under low-velocity and room temperature conditions, respectively. T is the assumed temperature (K), and $\dot{e}$ is the assumed strain rate (1/s).

The modelling of the turnbuckle stiffness that connects the ropes to the steel frame is also investigated in this study. While the detailed geometry of turnbuckles is not explicitly modelled, the parts corresponding to the turnbuckle attachments are rigidified to assess the effect of turnbuckle stiffness. Shared nodes are implemented at the end points of the ropes and the nodes outside the flange of the steel frame. Furthermore, the coupling condition between the ropes and the inside of the steel frame has been considered. In this study, two cases are considered: one in which the holes inside the flange of the steel frame are modelled and contact with the ropes (see Figure 3 a), and the other in which the nodes inside the flange of the steel frame and the nodes of the ropes are shared nodes at the initial placement position without modelling the holes (see Figure 3 b). In addition, the constraint conditions on the joint surface of the steel frame with the supporting columns are considered for the case of complete fixation (see Figure 4 a) and for the case in which the steel frame is allowed to rotate (see Figure 4 b). After applying gravity to the entire model and an initial tension to the ropes, the impactor placed at the centre of the net is given an initial velocity corresponding to a drop height of 3.5 m.

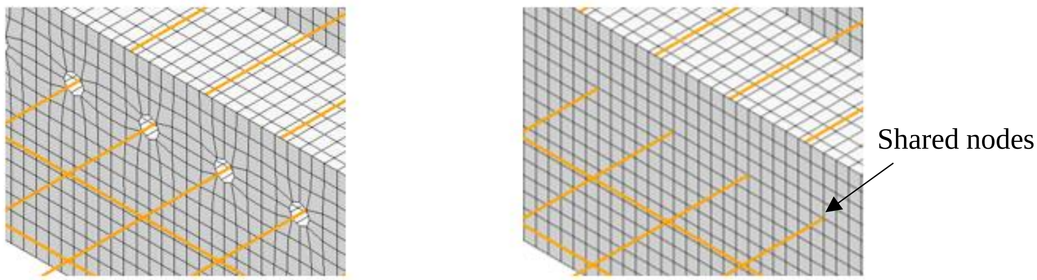

(a) Contact (b) Shared nodes

Figure 3. Coupling conditions between the ropes and the inside of the steel frame

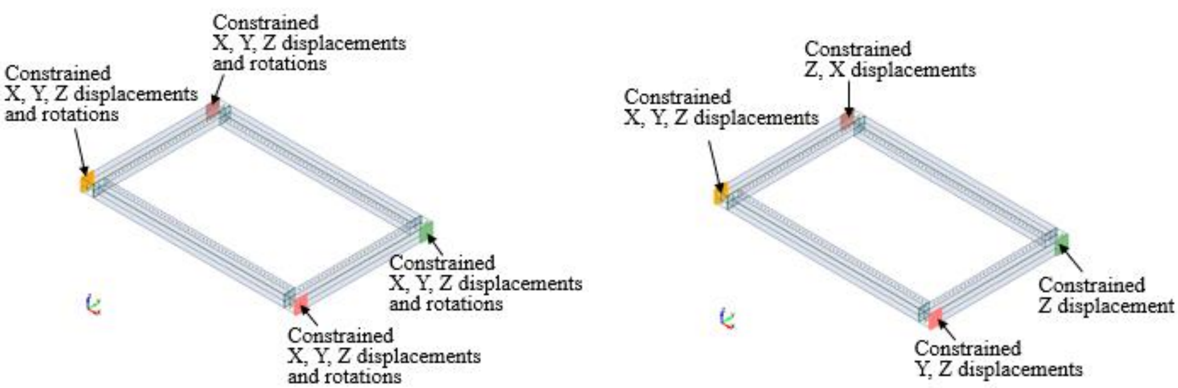

(a) Fixed (b) Allowed rotation

Figure 4. Constraint conditions of the steel frame

Results and comparison on modelling methods

The simulation case conditions and corresponding results for the maximum tension of ropes and impact load, when compared to Case 2, are shown in Table 2. Notably, Cases 3 and 4 have a larger difference compared to Case 2, which means that the effects of considering the strain rate dependency of the steel frame and the rigidification of the turnbuckles are significant.

Table 2: Simulation cases and results on modelling method

Case No.	Ropes	Steel frame	Boundary conditions			Simulation results	
	Compressive stiffness	Strain rate effects	Turnbuckle	Between the ropes and inside of the frame	Constraint conditions of the frame	Maximum tension of ropes [kN]	Impact load [kN]
1	Linear elastic	Included	Rigid	Contact	Allowed rotation	36.3 (+6%)	272.1 (+3%)
2	Neglected	Included	Rigid	Contact	Allowed rotation	34.3	265.2
3	Neglected	Excluded	Rigid	Contact	Allowed rotation	30.4 (-11%)	245.0 (- 8%)
4	Neglected	Included	Excluded	Contact	Allowed rotation	29.4 (-14%)	244.6 (- 8%)
5	Neglected	Included	Rigid	Shared nodes	Allowed rotation	36.1 (+5%)	267.6 (+1%)
6	Neglected	Included	Rigid	Contact	Fixed	35.5 (+3%)	273.7 (+3%)

(Rate of change against case 2)

Upon comparing Case 1 and Case 2 to assess the effect of compressive stiffness, it is observed that both the maximum tension of ropes and impact load are slightly higher in Case 1 than in Case 2. This is because the compressive stiffness of the ropes affects the tension distribution of the ropes as shown in Figure 5. In Case 1, the maximum tension distribution of the ropes is locally elevated near the inside of the steel frame, suggesting that the effect of the stiffness on the compression side may not have yielded a reasonable result. On the other hand, the tension distribution in Case 2, where the stiffness on the compression side of the ropes is neglected, exhibits a large tension at the point of impact with the weight, which is reasonable tension distribution.

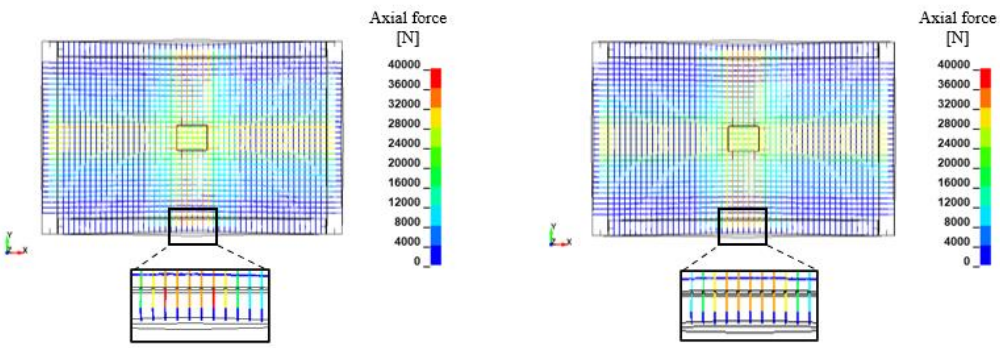

(a) Case 1 (b) Case 2

Figure 5. Maximum tension distribution of ropes (Case 1, Case 2)

Upon comparing Case 2 and Case 3 to assess the strain rate and plasticity of the steel frame, it is observed that both the maximum tension of ropes and impact load are smaller in Case 3 than in Case2. The time history of energies for Cases 2 and 3 is shown in Figure 6. In Case 2, where the steel frame is stiffened to consider strain rate dependence, there is a decrease in frame strain energy and an increase in rope strain energy compared to Case 3, where strain rate dependence is not considered. Furthermore, the consideration of strain rate dependency in the steel frame has led to an increased load distribution within the ropes.

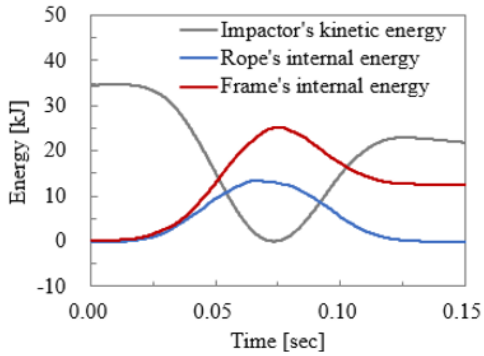

(a) Case 2

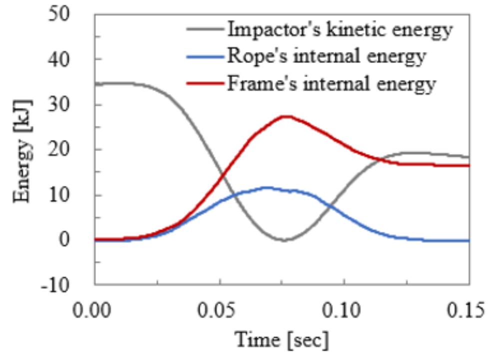

(b) Case 3

Figure 6. Time history of energies (Case2, Case3)

Upon comparing of Case 2 and Case 4 to assess the turnbuckle stiffness, it is observed that both the maximum tension of ropes and impact load are smaller in Case 4 than in Case2. The rope tension distribution is shown in Figure 7, indicating greater tension in Case 2 than in Case 4. It is assumed that the stiffness of the rope end increased due to the rigid turnbuckles, resulting in an increase in rope tension and impact load.

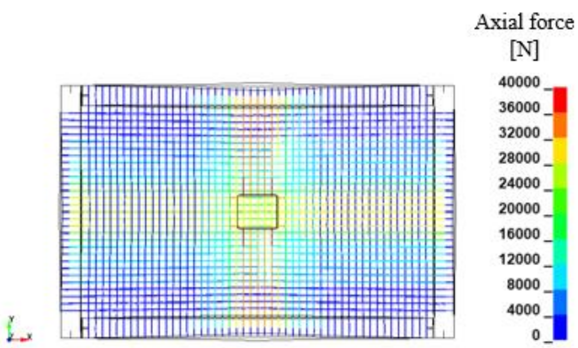

a) Case 2

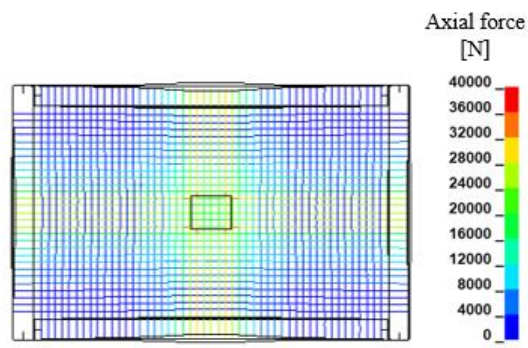

b) Case 4

Figure 7. Maximum tension distribution of ropes (Case 2, Case 4)

Upon comparing Case 2, Case 5, and Case 6 to assess boundary conditions, it is observed that the difference is within 5% for both the maximum tension of ropes and impact load. This suggests that the coupling conditions between the ropes and the inside of the steel frame, and the steel frame restraints have little effect on the results. By modelling the ropes and the steel frame with shared nodes, it is possible to model the nets as shell finite elements rather than beam finite elements. Shell finite elements offer the advantage of allowing more material models to be used compared to beam elements, as well as the ability to model sheet shapes other than nets.

STUDY ON PROTECTIVE STRUCTURES

To compare the energy absorption effects of different materials in protective structures, a comparative study has been conducted using simulation based on the protective rope net made of aramid fibre, as shown in Figure 2.

Component selection and modelling

Steel plates have been used at the Onagawa nuclear power plant and other nuclear power plants (Tohoku Electric Power Co., Inc, 2021). Implement of composite panels made of steel plates and aramid fibre sheets are being discussed in Joyo, the experimental fast reactor (Japan Atomic Energy Agency, 2022). Aramid fibre sheets have been proposed as a reinforcement solution for volcanic eruptions because they are lightweight, higher tensile strength than steel plates, and have excellent corrosion resistance (Cabinet Office, 2015). In this study, the aramid fibre rope net in the simulation is replaced with a steel plate or an aramid fibre sheet as shown in Figure 8 to compare their energy absorption effects.

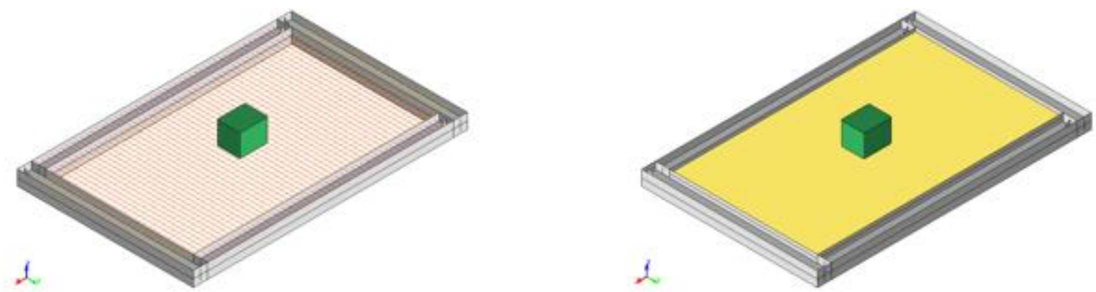

(a) Aramid fibre rope net　　　(b) Steel plate or Aramid fibre sheet

Figure 8. Simulation model for the rope net or sheets

The aramid fibre rope net is modelled using beam finite elements, with the intersections of the ropes represented as shared nodes. The material model for the ropes is an elastic spring model, and the stiffness on the compression side is neglected. The turnbuckles are modelled as rigid parts, as mentioned above.

The steel plate is modelled using shell finite elements. The material of the steel plate is SS400, as used the Onagawa power plant, and isotropic elastoplastic material is applied to account for strain rate dependence in the same manner as for the steel frame. The steel plate thickness is 1.4 mm, determined using the BRL formula in Equation 2, which is used as the evaluation formula for steel plate penetration in the Guidelines for Tornado Missile (JSME S NX6-2019).

$$\left(\frac{T}{D}\right)^{1.5} = \frac{0.5MV^2}{1.44\times10^9 K_S^2} \tag{2}$$

where T is the critical thickness for penetration (m), M is the volume of impactor (kg), V is the impact velocity (m/s), K_S is a coefficient depending on the grade of steel (usually 1.0); D is effective diameter of the impactor (m), which is determined based on the contact area considering the shape of the impactor.

The aramid fibre sheet is modelled using membrane finite elements without consideration of bending stiffness. The fibre material model is used, and material property values obtained from tensile and in-plane shear tests (Public Works Research Institute et al., 2021) are applied. The thickness of the aramid fibre sheet is 1.4 mm, the same as that of the steel plate.

Since the coupling condition between the ropes and the inside of the steel frame has been found to have a small effect on the simulation results, the inside of the steel frame is modelled as shared with each node of the ropes or the sheets. The steel frame restrains allow for rotation (see Figure 4 b). Before the impactor is dropped, gravitational acceleration is applied to the protective structures and the steel frame, and the ropes are also subjected to initial tension. After obtaining a static state due to gravity and initial tension, an initial velocity is applied to the centrally placed impactor for a height of 3.5 m.

Comparison of energy absorption

The simulation results, including the maximum impact load on the impactor, the maximum displacement of the protective structure, and the amount of energy absorption up to the time of maximum displacement compared to the aramid fibre rope net are shown in Table 3. The relationship between impact load and displacement is also shown in Figure 9. The aramid fibre rope net exhibits the smallest impact load among the three, but it also has the largest displacement. Conversely, the steel plate has the smallest displacement, but generates a larger load immediately after impact, resulting in the largest impact load among the three. The impact load and displacement of the aramid fibre sheet fall between those of the aramid fibre rope net and the steel plate, with comparable energy absorption in each case.

Table 3: Simulation results on protective structures

Protective structures	Impact load [kN]	Displacement [mm]	Energy absorption [J]
Aramid fiber rope net	267	437	38600
Steel plate	285 (+7%)	313 (-28%)	37300 (-3%)
Aramid fibre sheet	271 (+1%)	390 (-11%)	38200 (-1%)

(Rate of change against Aramid fibre rope net)

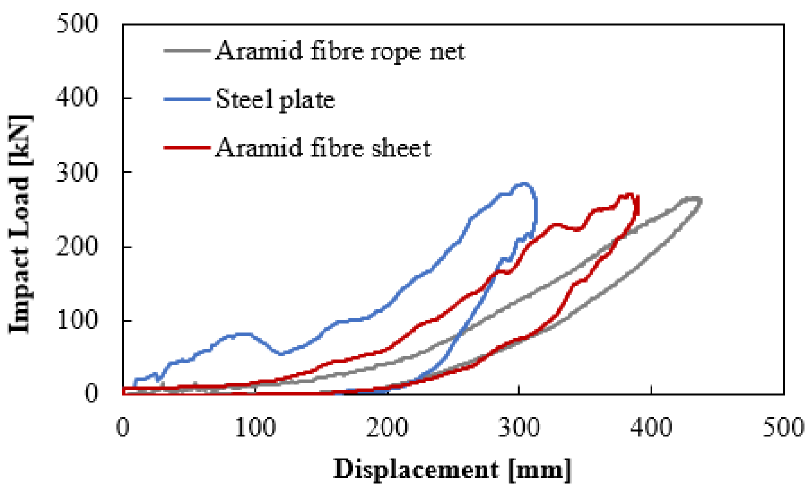

Figure 9. History of impact road and displacement

Mechanical state of protective structures

The aramid fibre rope net has a maximum axial force of 39700 N at the impactor impact point, which is below the rope's specified strength of 46100 N (Aizawa et al.), as shown in Figure 10.

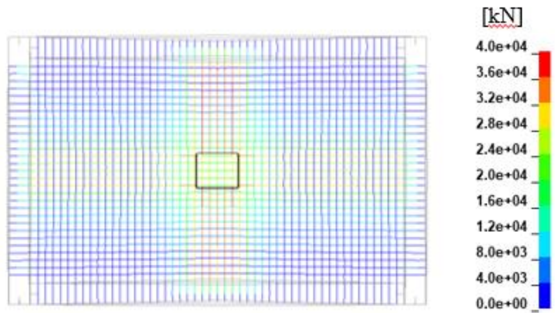

Figure 10. Axial force distribution of aramid fibre rope at maximum displacement

The steel plate has tensile stress distributed from the impact point of the impactor to the corner of the frame (see Figure 11 a). The criterion for evaluating the fracture of a steel plate is the state in which the effective plastic strain is equal to the limit value of the local effective plastic strain ε_L, defined as follow (JSME S NX6-2019):

$$\varepsilon_L = \varepsilon_{Lu} \cdot exp\left[-\left(\frac{\alpha_{sl}}{1+m_2}\right)\left(\left\{\frac{TF}{3} - \frac{1}{3}\right\}\right)\right] \tag{3}$$

$$\varepsilon_{Lu} = m_2 = 0.60 \cdot (1.00 - R), \quad \alpha_{sl} = 2.2 \qquad \text{for ferritic steel}$$

$$R = \frac{S_y}{S_u}$$

where TF is the stress triaxiality factor ranging from -2 to +2 in shell finite elements, ε_{Lu} is the strain value at tensile strength, S_y is the yield stress of the material specification, and S_u is the tensile strength of the material specification. The maximum effective plastic strain of the steel plate is 0.08 at the impact point of the impactor (see Figure 11 b), which is lower than the fracture criterion ε_L=0.128.

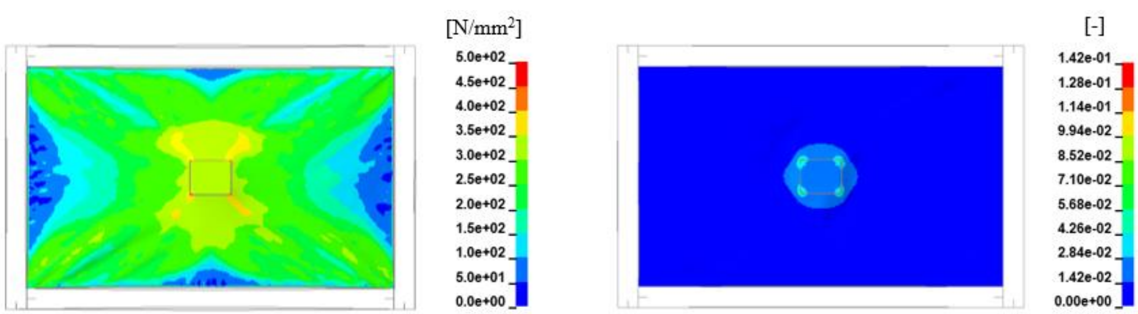

(a) Maximum principal stress (b) Effective plastic strain

Figure 11. Maximum principal stress distribution at maximum displacement,
and effective plastic strain distribution at the end of the simulation of the steel plate

Since the fracture criterion for aramid fibre sheets is not as clear as for steel sheets, a comparison is made based on tensile strength and shear strength (Public Works Research Institute et al., 2021). The maximum tensile stress of 995 MPa occurred at the corner of the impact point of the impactor (see Figure 12 a), which is below the tensile strength of 2500 MPa. However, the shear stress across the entire sheet exceeds the shear strength of 34 MPa (see Figure 12 b).

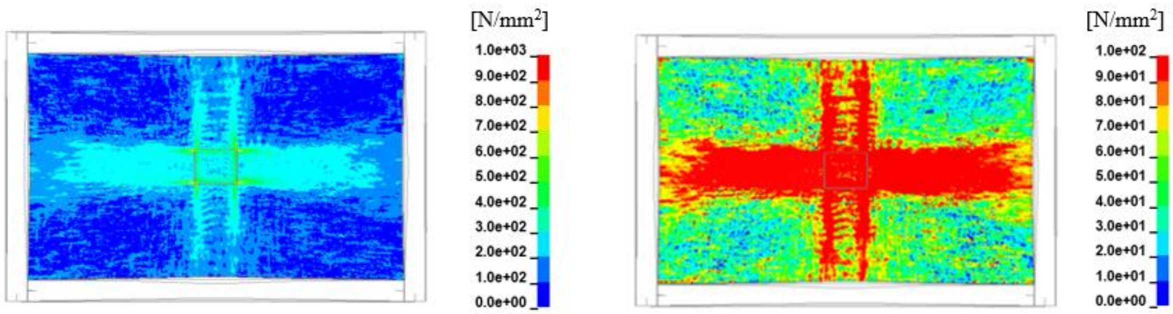

(a) Maximum principal stress (b) Maximum share stress

Figure 12. Maximum principal stress and maximum share stress distribution at maximum displacement of the aramid fibre sheet

Comparison of the steel plate stress

The same criterion for evaluation of steel frame fracture, ε_L=0.128 in Equation 3 as for steel plates, is applied. The effective plastic strain of the steel frame is the largest for the case of aramid fibre rope, which has the largest deformation, and the smallest for the case of steel plate, which has the smallest deformation, as shown in Figure 13. The maximum values of effective plastic strain are 0.019 for the case of aramid fibre rope, 0.005 for the case of steel plate, and 0.016 for the case of aramid fibre sheet, all below ε_L.

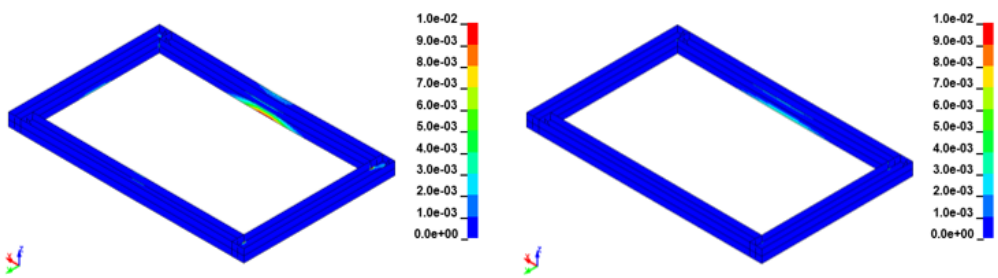

(a) Aramid fibre rope net (b) Steel plate

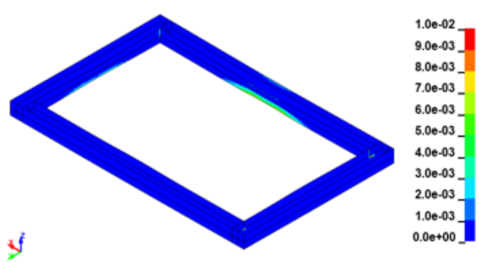

(c) Aramid fibre sheet

Figure 13. Effective plastic strain distribution at the end of the simulation of the steel frame

CONCLUSION

The crash simulation model for the member of flexible structure has been studied, and the following conclusions were drawn. The material model of the ropes is reasonable without considering the stiffness on the compression side, and it is crucial to consider the strain rate dependence of the steel frame and the rigidification of the turnbuckles. On the other hand, the effects of the coupling conditions between the steel frame and the protective structures and the frame restraint conditions are small.

Applying the studied modelling method, a comparison has been made regarding the energy absorption of different flexible protective structures. The simulation results indicated that all structures absorbed the same amount of energy. The steel sheet exhibited the smallest deformation and imposed the least load on the steel frame. However, aramid fibre sheets may need reinforcement through composite panels or other means because shear stresses above the shear strength of the aramid fibre sheets alone are expected to cause them to rupture. Since the energy absorption for all cases investigated above is almost the same, aramid fibre components may be advantageous from a weight perspective. This is crucial because building or other structures that need protection from tornado flying objects or volcanoes eruptions must also pass capability checks for earthquakes.

REFERENCES

Aizawa, K., Ishimaru, M., Maeda, S., Okada, T., Matsui, H., Kumagai, Y., Isaka, S. (2021). “Development of protective net using high strength lightweight aramid for tornado missile,” *Proc., the 17th annual conference*, Japan Society of Maintenology.

Cabinet Office (Disaster Prevention). (2015). *Guidance for the Improvement of Evacuation Shelters, etc. at Active Volcanoes*, JP.

Japan Atomic Energy Agency. (2022). *Article 6 (Prevention of damage from external impacts) (Part 4: Tornadoes),* JP.

Kiyota, S., Kataoka, S., Beppu, M., Ichino, H., Sato, K. (2020). “Mitigation effects by aramid fibre sheets reinforcement on the scabbing of RC slabs,” *Journal of structural engineering,* Japan Society of Civil Engineers, Vol. 66A.

Public Works Research Institute, Japan Association for Fibre Repair and Strengthening, Sekisui Chemical Co., Ltd. (2021). “Joint Research Report of Durability Evaluation of Continuous Fibre Reinforced RC Slabs (I) - Examination of Shear Modulus of Continuous Fibre Sheets -,” *Joint Research Report*, No. 522.

The American Society of Mechanical Engineers. (2019). *Boiler and Pressure Vessel Code*, Section VIII, Division 2, Annex3-D.

The Japan Society of Mechanical Engineers. (2019). *Codes for Nuclear Power Generation Facilities - Guidelines for Structural Integrity Evaluation Method due to Load of Tornado Missile* -, JSME S NX6-2019.

The Japan Welding Engineering Society. (2017). *Method of assessing brittle fracture in steel weldments subjected to large cyclic and dynamics strain*, WES 2808.

Tohoku Electric Power Co., Inc. (2021). *Onagawa nuclear power plant No. 2 unit Construction plan review document*, JP.